

Tuning the structure and magnetic properties via distinct pyridine derivatives in cobalt(II) coordination polymers

Dong Shao,^{*a} Shruti Moorthy,^b Xiaodong Yang,^a Jiong Yang,^c Le Shi,^d Saurabh Kumar Singh,^{*b} Zhengfang Tian^a

^a Hubei Key Laboratory of Processing and Application of Catalytic Materials, College of Chemistry and Chemical Engineering, Huanggang Normal University, Huanggang 438000, P. R. China

^b Department of Chemistry, Indian Institute of Technology Hyderabad, Kandi-502285, Sangareddy, Telangana, India

^c Department of Chemistry, Southern University of Science and Technology, Shenzhen 518055, P. R. China

^d Faculty of Chemistry, Jagiellonian University, 30387 Kraków, Poland

Correspondence and requests for materials should be addressed to

Email: shaodong@nju.edu.cn (D. S.) or sksingh@chy.iith.ac.in (S. K. S.)

Table of Content

Experimental Section	4
Figure S1. The asymmetric units of 1 and 2	7
Table S1. Selected bond lengths (Å) and angles [°] for 1	8
Table S2. Selected bond lengths (Å) and angles [°] for 2	9
Table S3. Continuous Shape Measure analysis for 1 and 2	10
Figure S2. Packing diagram of the neutral one-dimensional coordination chain of 1	11
Figure S3. A portion of the packing crystal structure of three-dimensional coordination framework of 2 along two main crystallographic axes: the b axis (a) and the c axis (b)..	12
Figure S4. A portion of the topology structure of two-dimensional coordination layer of 2 along two main crystallographic axes: the a axis (a) and the b axis (b).	13
Figure S5. Comparison of the experimental PXRD patterns of 1 and 2 with the simulated patterns from their single crystal structures.	14
Figure S6. Thermogravimetric curves of 1 and 2 measured under the nitrogen atmosphere upon the continuous heating with the $10\text{ }^{\circ}\text{C}\cdot\text{min}^{-1}$ rate.....	15
Figure S7. Variable-temperature magnetic susceptibility for 2	16
Figure S8. Variable-temperature magnetic susceptibility for 1 (up) and 2 (down).....	17
Figure S9. Frequency dependence of the in-phase (χ') and out-of-phase (χ'') ac susceptibilities measured under zero dc field at 1.8 K for 1 and 2	18
Figure S10. Frequency dependence of the in-phase (χ') and out-of-phase (χ'') part of the ac susceptibilities measured under various dc fields at 1.8 K for 1 and 2	19
Figure S11. Cole-cole plot for 2 under various dc fields at 1.8 K.....	20
Table S4. Relaxation fitting parameters at 1.8 K under different fields from the least-square fitting of the Cole-Cole plots of 2 according to the generalized Debye model.....	21
Figure S12. Field dependence of the magnetic relaxation time at 1.8 K for 2 and its approximation by $\tau^{-1} = AH^2T + B_1/(1 + B_2H^2)$	21
Figure S13. Temperature dependence of the in-phase (χ') and out-of-phase (χ'') part of the ac susceptibilities measured under 1 kOe dc field for 2	22
Figure S14. Cole-cole plot for 2 under various dc fields at 1.8 K.....	23
Table S5. Relaxation fitting parameters from the least-square fitting of the Cole-Cole plots of 2 according to the generalized Debye model.....	24
Figure S15. Monomeric (top) and Dimeric (bottom) models extracted from the crystal structure of complexes 1 and 2	25
Table S6. CASSCF/NEVPT2 computed 10 spin-free quartets (red) and 40 spin-free doublet (black) states along with the spin-orbit states for 1a.....	26
Table S7. CASSCF/NEVPT2 computed 10 spin-free quartets (red) and 40 spin-free doublet (black) states along with the spin-orbit states for 2a.....	27
Figure S16. Orientation of computed effective g-tensor of complex 1a and 2a.	28
Figure S17. Orientation of computed D-tensor of complex 1a and 2a.	28
Figure S18. Experimental and <i>ab initio</i> computed magnetic susceptibility plots for complexes (a) 1 and (b) 2	29
Figure S19. Experimental and <i>ab initio</i> computed magnetization curves at 2K (a) 1 and (b) 2 . The black squares represent the experimental values, and the blue and red lines correspond to	

CASSCF and NEVPT2 computed values. All these computed values are obtained from the calculations on monomeric model complexes 1a and 2a	29
Table S8. CASSCF (7,5)+NEVPT2 computed Spin–Hamiltonian parameter (g , D , $ E/D $) parameters along with wavefunction decomposition analysis.	30
Table S9. AILFT derived ligand field parameters computed at CASSCF (in parentheses) and NEVPT2 level of theory for model complexes 1a and 2a.	31
Table S10. BS-DFT computed energies of high-spin and broken-symmetry solution of complex 1b using $H=-JS_1S_2$ formalism.	32
Table S11. BS-DFT computed energies of high-spin and broken-symmetry solution of complex 2b using $H=-JS_1S_2$ formalism.	33
Figure S20. DFT calculated spin-density plot for the ground state ($S=0$) of complexes 1b and 2b	34
Figure S21. DFT calculated overlap integrals for complexes (a) 1b and (b) 2b.	35
Reference	36

Experimental Section

General Procedure. Infrared (IR) spectra data were measured on KBr pellets using a Nexus 870 FT-IR spectrometer in the range of 4000-400 cm⁻¹. Elemental analyses of C, H, and N were performed at an Elementar Vario MICRO analyzer. Powder X-ray diffraction data (PXRD) were recorded at room temperature on a Bruker D8 Advance diffractometers with Cu K α X-ray source ($\lambda = 1.54056 \text{ \AA}$) operated at 40 kV and 40 mA. Thermal gravimetric analysis (TGA) was measured in Al₂O₃ crucibles using a PerkinElmer Thermal Analysis in the temperature range of 20-800 °C under flowing nitrogen at a heating rate of 10 °C/min.

Magnetic Measurements. Magnetic susceptibility measurements from 2 to 300 K with dc field up to 70 kOe were performed using a Quantum Design SQUID VSM magnetometer on the grounded powders from the single crystals of the compounds. Alternative current (ac) magnetic susceptibility data were collected in a zero direct current (dc) field or various dc fields in the temperature range of 2-8 K, under an ac field of 2 Oe, oscillating at frequencies in the range of 1-1000 Hz. All magnetic data were corrected for the diamagnetism of the sample holder and of the diamagnetic contribution of the sample using Passcal's constants.

X-ray Crystallography. Single crystal X-ray crystallographic data were collected on a Bruker D8 Venture diffractometer with a CCD area detector (Mo-K α radiation, $\lambda = 0.71073 \text{ \AA}$) at 153 or 112 K. The unit cell parameters and data collection were determined by the APEXII program. The data were integrated and corrected for Lorentz and polarization effects using SAINT.¹ Absorption corrections were applied with SADABS.² The structures were solved by direct methods and refined by full-matrix least-squares method on F^2 using the SHELXTL³ crystallographic software package integrated in Olex 2.⁴ All the non-hydrogen atoms were refined anisotropically. Hydrogen atoms of the organic ligands were refined as riding on the corresponding non-hydrogen atoms. Additional details of the data collections and structural refinement

parameters are provided in Table 1. Selected bond lengths and angles of **1** and **2** are listed in Table S1 and S2. CCDC 2085411 and 2085412 are the supplementary crystallographic data for this paper. They can be obtained freely from the Cambridge Crystallographic Data Centre via www.ccdc.cam.ac.uk/data_request/cif.

Computation methods. All calculations were carried out using ORCA 4.2.1 suite of programs.^{5,6} To extract the zero-field splitting parameters, g-value in complexes **1** and **2**, we have prepared a monomeric model of both the complexes called **1a** and **2a** (see Figure S13). Later, the position of hydrogens was optimized using the BP86 level of theory^{7,8} with DKH-def2-TZVP⁵ basis set for Co, Cl, N, and O and DKH-def2-SVP⁵ for the rest of the atoms. The calculation of electronic, magnetic properties and spin-Hamiltonian parameters (g, D, E) of complexes **1a** and **2a** were computed by complete active space self-consistent (CASSCF) method with an active space of CAS (7, 5) i.e., seven active electrons in the five active d-orbitals of Co(II). Using this active space, we have computed 10 quartets and 40 doublets states. All these calculations were carried out with a DKH-def2-TZVPP⁹ basis set for all atoms. To treat the dynamic correlations, the second-order N-electron valence perturbation theory (NEVPT2) method was employed on the converged CASSCF wavefunction. Ab-initio based ligand field theory (AILFT) analysis was carried out to analyze the nature of ligand field and d-orbital splitting as implemented in ORCA.

To compute the isotropic exchange coupling between the Co(II) centers in complexes **1** and **2**, we have prepared a dimeric model of both complexes called as **1b** and **2b** (see Figure S13). The position of hydrogens in both complexes **1b** and **2b** were optimised. Scalar relativistic DFT calculations with B3LYP functional¹⁰ including Grimme's dispersion correction (D3BJ)^{11,12} were performed to compute the isotropic exchange coupling. The isotropic exchange coupling was calculated using the broken symmetry formalism¹³ where the energy of broken-symmetry solutions is obtained by flipping spin on one of the Co(II) centres. The broken-symmetry solutions were verified by analyzing the nature of the spin density (spin-flip). Scalar relativistic effects were

accounted by employing Douglas-Kroll-Hess (DKH) approximation. All electron DKH-def2-TZVP⁹ basis set was employed for all atoms as implemented in ORCA. RIJCOSX¹⁴ approximation was used to speed up the calculations. The J values are calculated using the formulation proposed by Ruiz et al. (see equation 1), which has proven robust in computing J values in various transition metal complexes.¹⁶⁻²¹

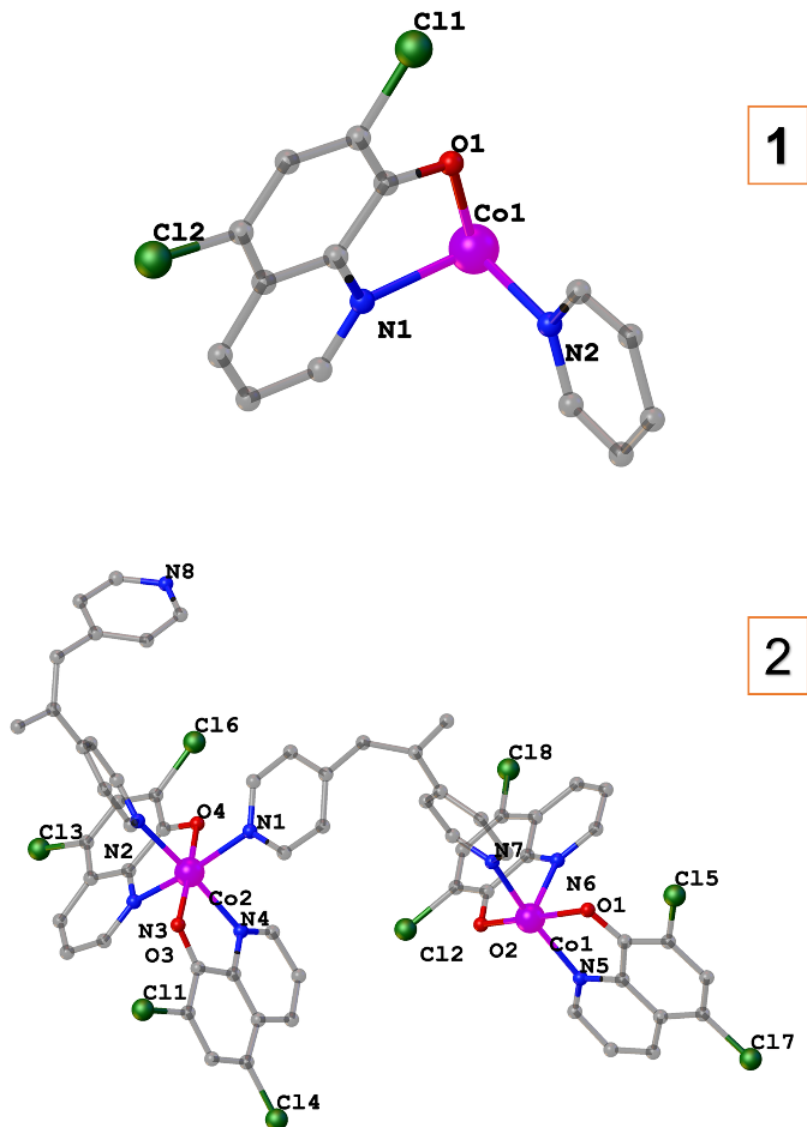


Figure S1. The asymmetric units of **1** and **2**.

Table S1. Selected bond lengths (\AA) and angles [$^\circ$] for **1**.

parameter	Value / \AA , $^\circ$
Co1-O1	2.0544(12)
Co1-O1*	2.0544(12)
Co1-N1*	2.1083(15)
Co1-N1	2.1083(15)
Co1-N2*	2.1711(14)
Co1-N2	2.1711(14)
Co-N/O _{average}	2.111
O1-Co1-O1*	180.0
N1-Co1-N1*	180.00 (7)
O1*-Co1-N1*	80.19(5)
O1-Co1-N1 ¹	99.82(5)
O1*-Co1-N1	99.81(5)
N2-Co1-O1	89.89(5)
Symmetry transformations used to generate equivalent atoms:	
* 1-X,1-Y,1-Z	

Table S2. Selected bond lengths (\AA) and angles [$^\circ$] for **2**.

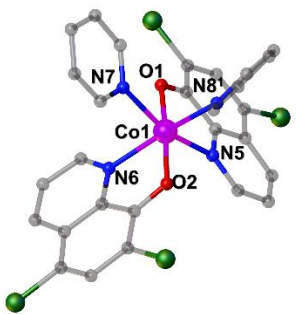
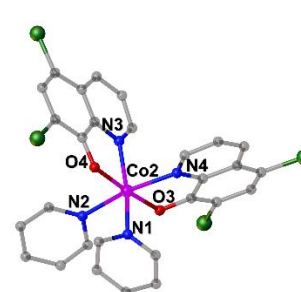
parameter	Value / \AA , $^\circ$
	
Co1-O1	2.051(3)
Co1-O2	2.037(3)
Co1-N5	2.148(3)
Co1-N6	2.156(3)
Co1-N7	2.155(3)
Co1-N8 ¹	2.177(3)
Co1-N/O _{average}	2.121
	
Co2-O3	2.035(2)
Co2-O4	2.033(3)
Co2-N1	2.140(4)
Co2-N2	2.177(4)
Co2-N3	2.139(4)
Co2-N4	2.156(5)
Co2-N _{average}	2.113
O1-Co1-N5	78.31(12)
O1-Co1-N6	95.01(13)
O1-Co1-O8 ¹	84.80(13)
O2-Co1-O1	171.64(11)
O2-Co1-O5	97.40(12)
O3-Co2-O1	98.80(12)
Symmetry transformations used to generate equivalent atoms:	
¹ 1+X,+Y,+Z	

Table S3. Continuous Shape Measure (CSM) analysis for six-coordinated Cobalt(II) in **1** and **2**.

Compound, Metal center	CSM parameters*					Determined coordination geometry	
	six-coordinated coordination sphere						
	HP-6	PPY-6	OC-6	TPR-6	JPPY-6		
1	30.042	29.595	7.944	18.822	30.918	OC-6	
2_Co1	28.861	20.762	3.711	9.184	23.174	OC-6	
2_Co2	25.169	23.994	3.954	13.441	25.091	OC-6	

* CSM²² parameters for six-coordinated complexes:

HP-6 - the parameter related to the hexagon (D_{6h})

PPY-6 - the parameter related to the pentagonal pyramid (C_{5v})

OC-6 - the parameter related to the octahedron (O_h)

TPR-6 - the parameter related to the trigonal prism (D_{3h})

JPPY-6 - the parameter related to the Johnson pentagonal pyramid (C_{5v})

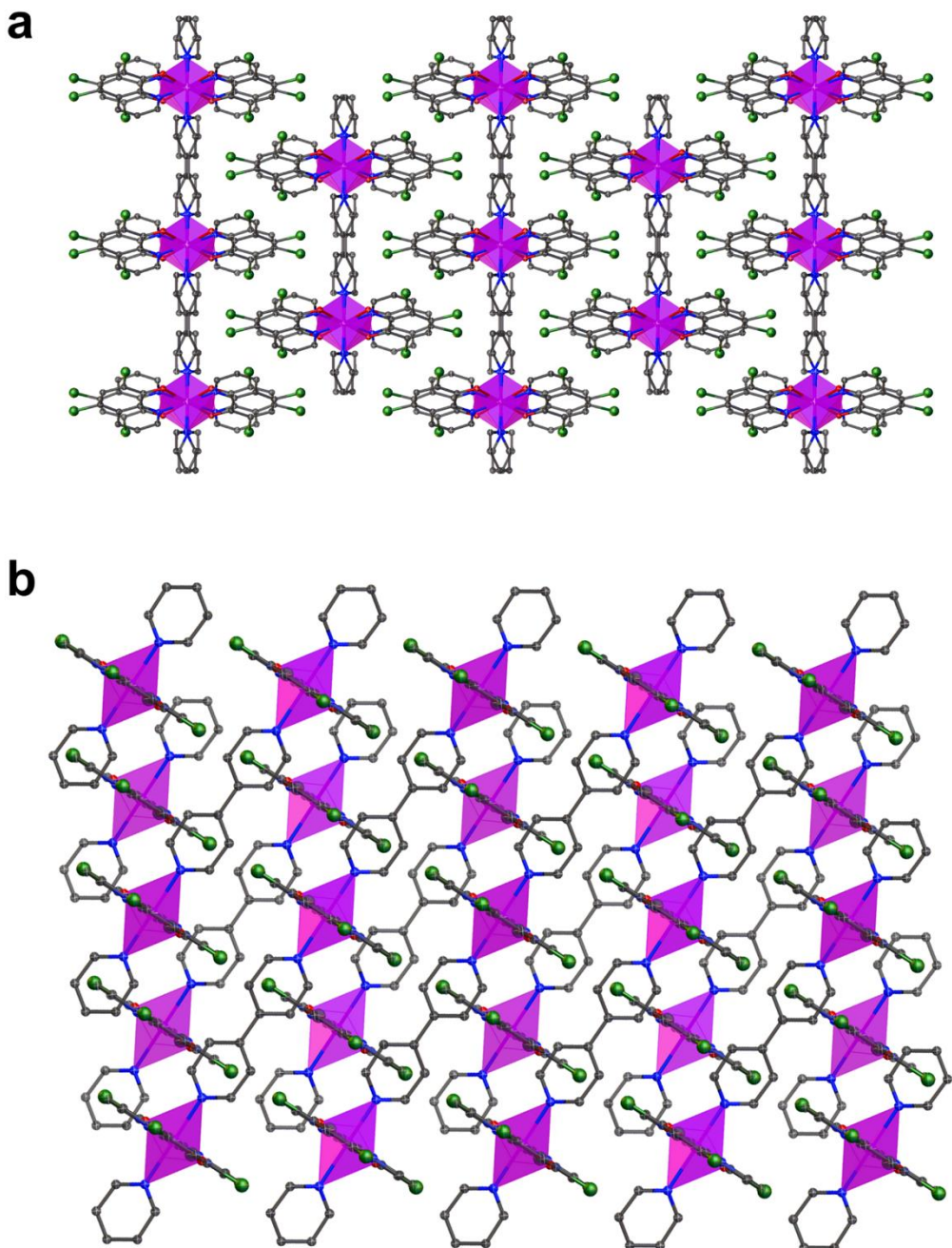


Figure S2. Packing diagram of the neutral one-dimensional coordination chain of **1** along two main crystallographic axes: the **c** axis (**c**) and the **b** axis (**b**).

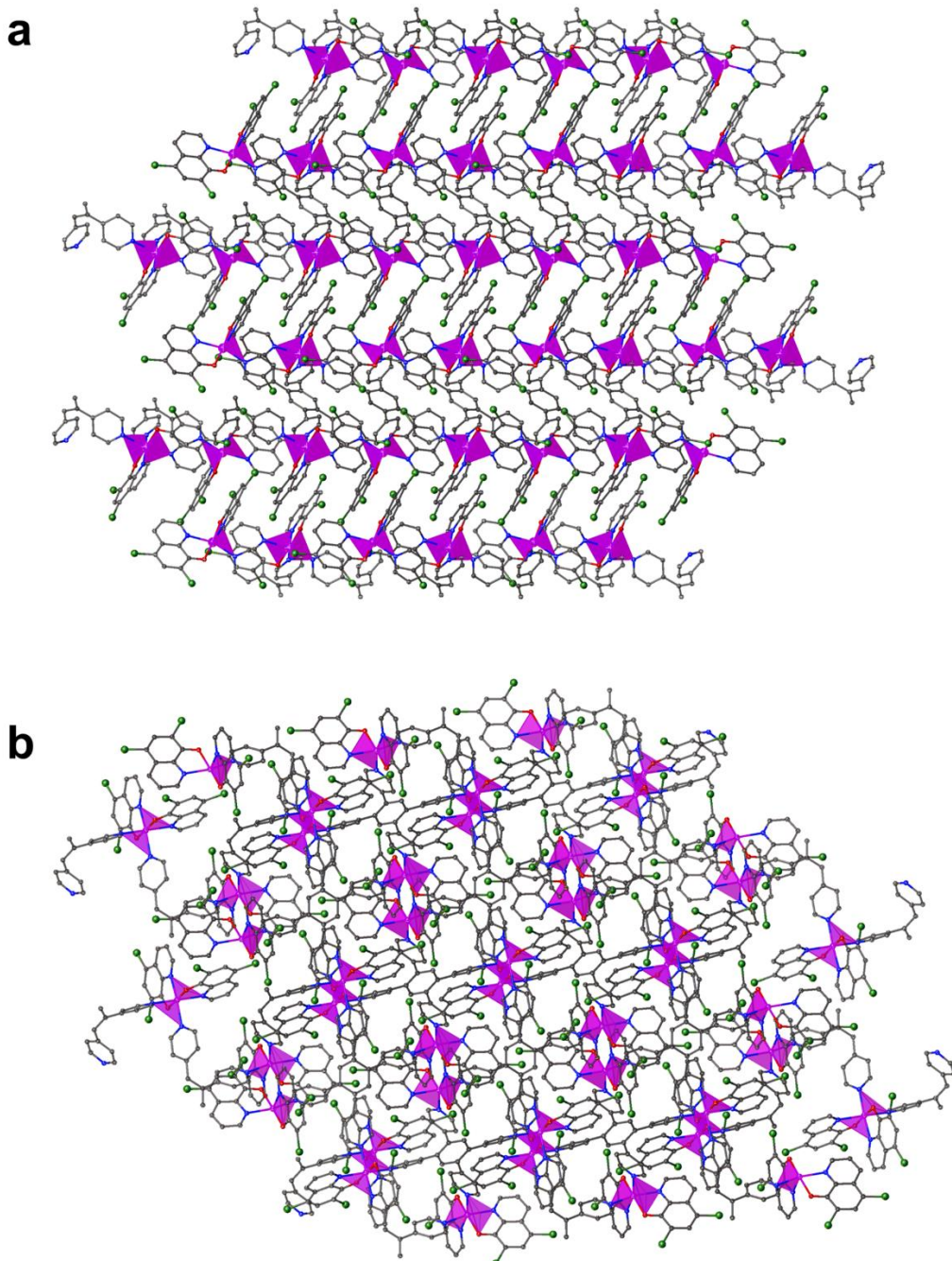


Figure S3. A portion of the packing crystal structure of three-dimensional coordination framework of **2** along two main crystallographic axes: the **b** axis (a) and the **c** axis (b).

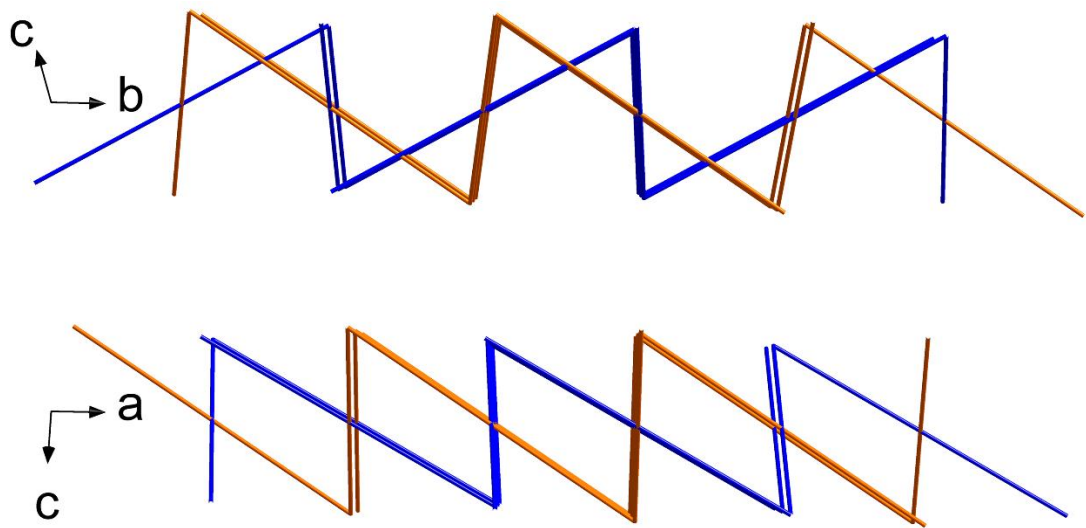


Figure S4. A portion of the topology structure of two-dimensional coordination layer of **2** along two main crystallographic axes: the **a** axis (**a**) and the **b** axis (**b**).

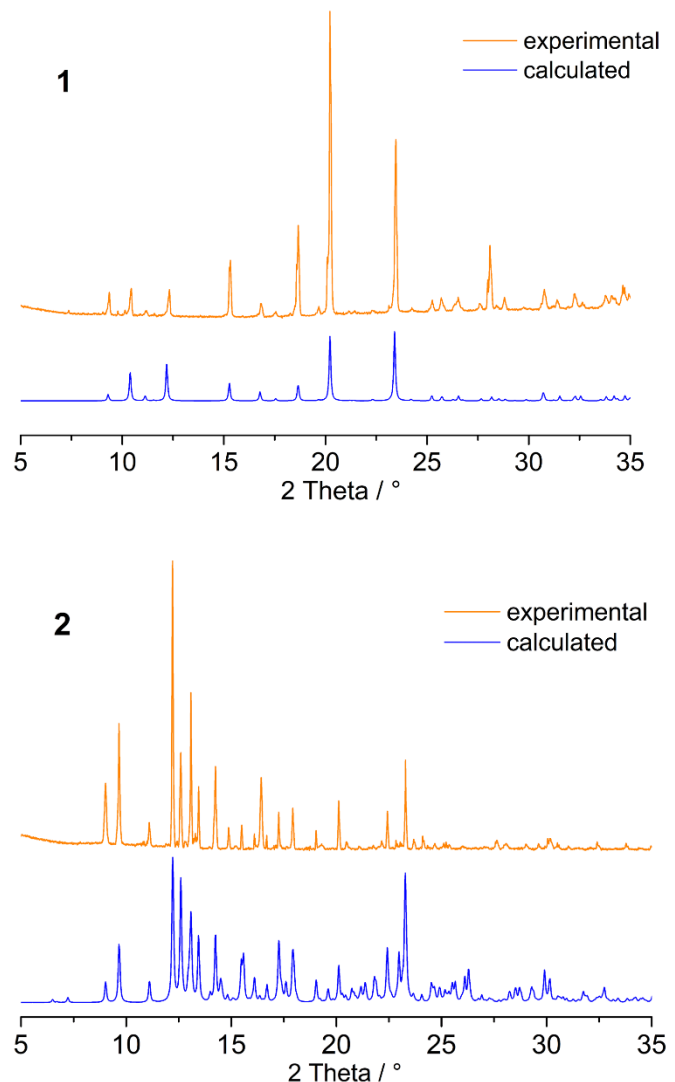


Figure S5. Comparison of the experimental PXRD patterns of **1** and **2** with the simulated patterns from their single crystal structures. The calculated patterns were generated from Mercury using the CIF of the crystal structure.

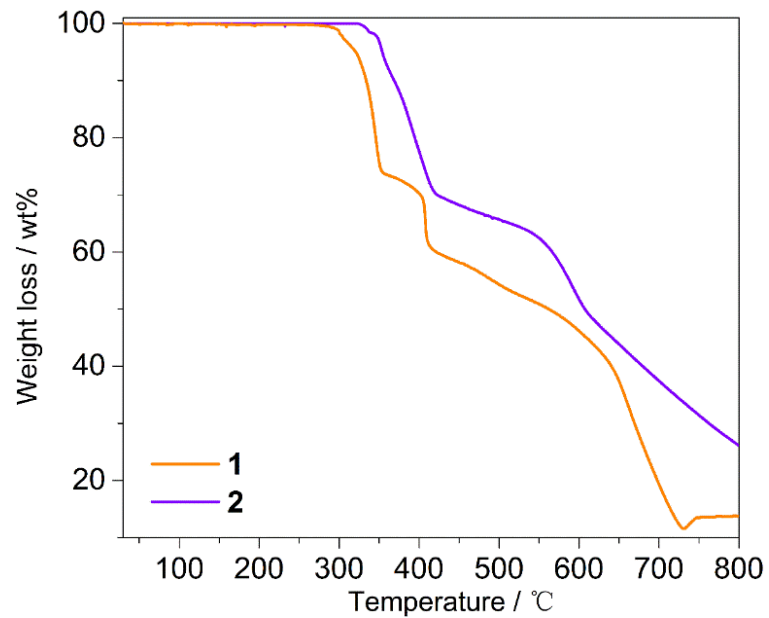


Figure S6. Thermogravimetric curves of **1** and **2** measured under the nitrogen atmosphere upon the continuous heating with the $10\text{ }^{\circ}\text{C}\cdot\text{min}^{-1}$ rate.

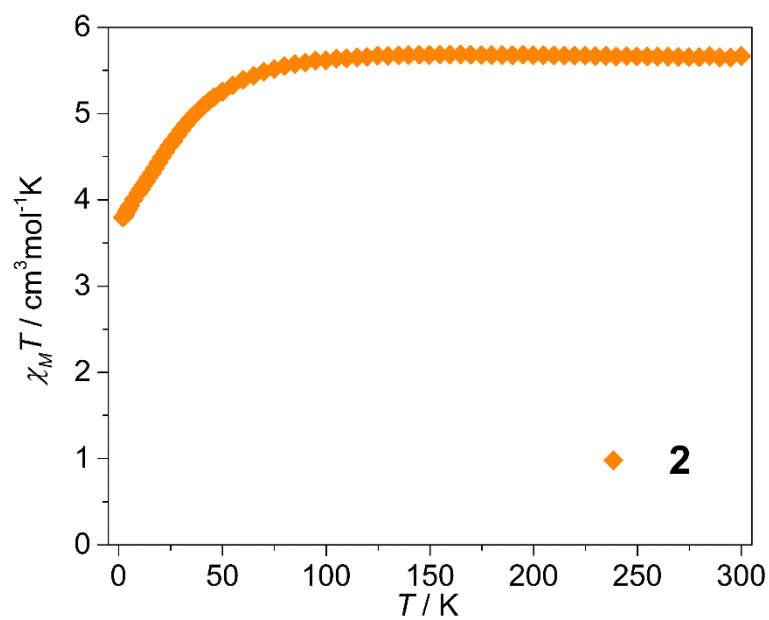


Figure S7. Variable-temperature magnetic susceptibility for **2** measured under 1 kOe dc field.

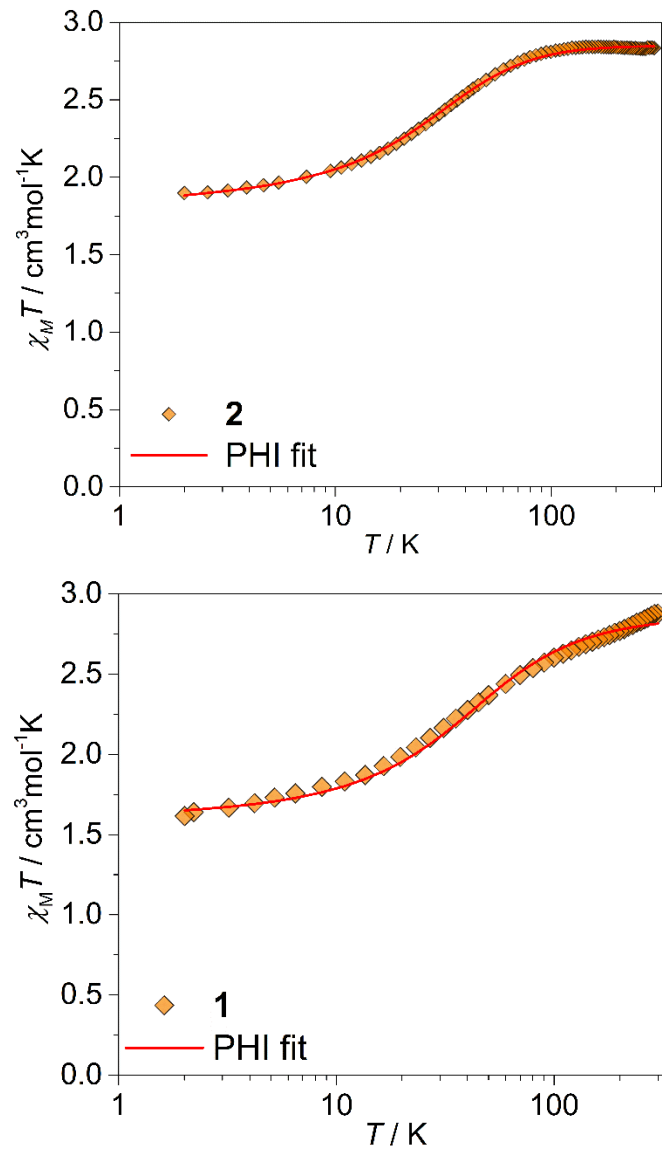


Figure S8. Variable-temperature magnetic susceptibility for **1** (up) and **2** (down) measured under 1 kOe dc field.

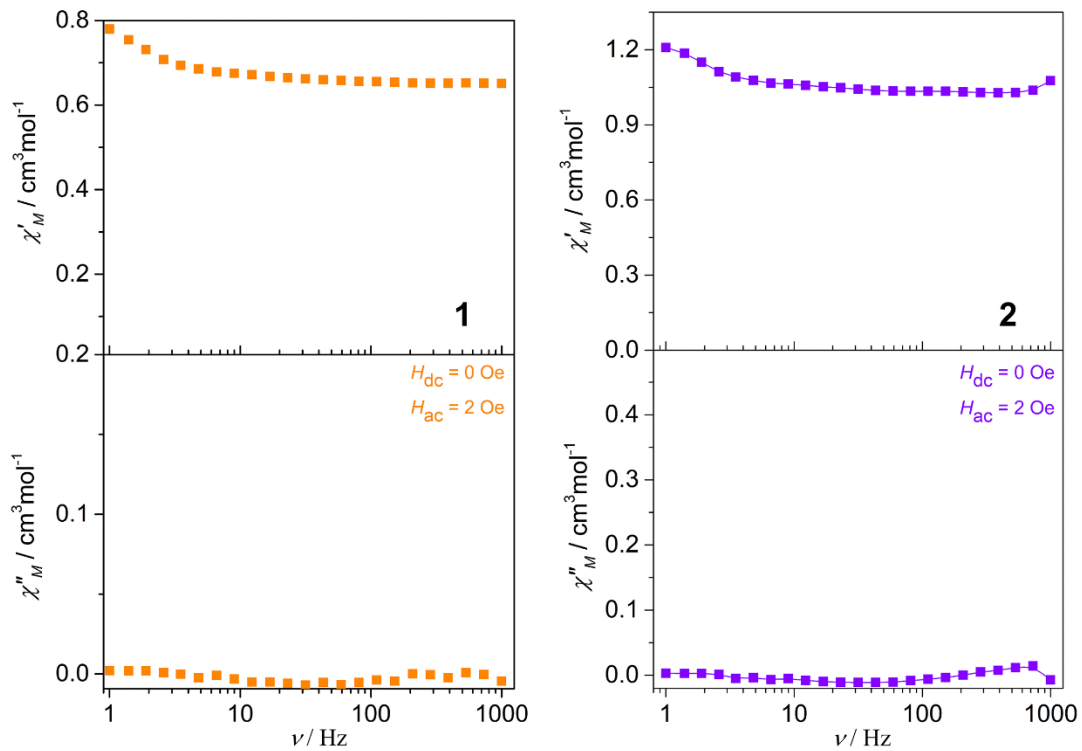


Figure S9. Frequency dependence of the in-phase (χ') and out-of-phase (χ'') ac susceptibilities measured under zero dc field at 1.8 K for **1** and **2**.

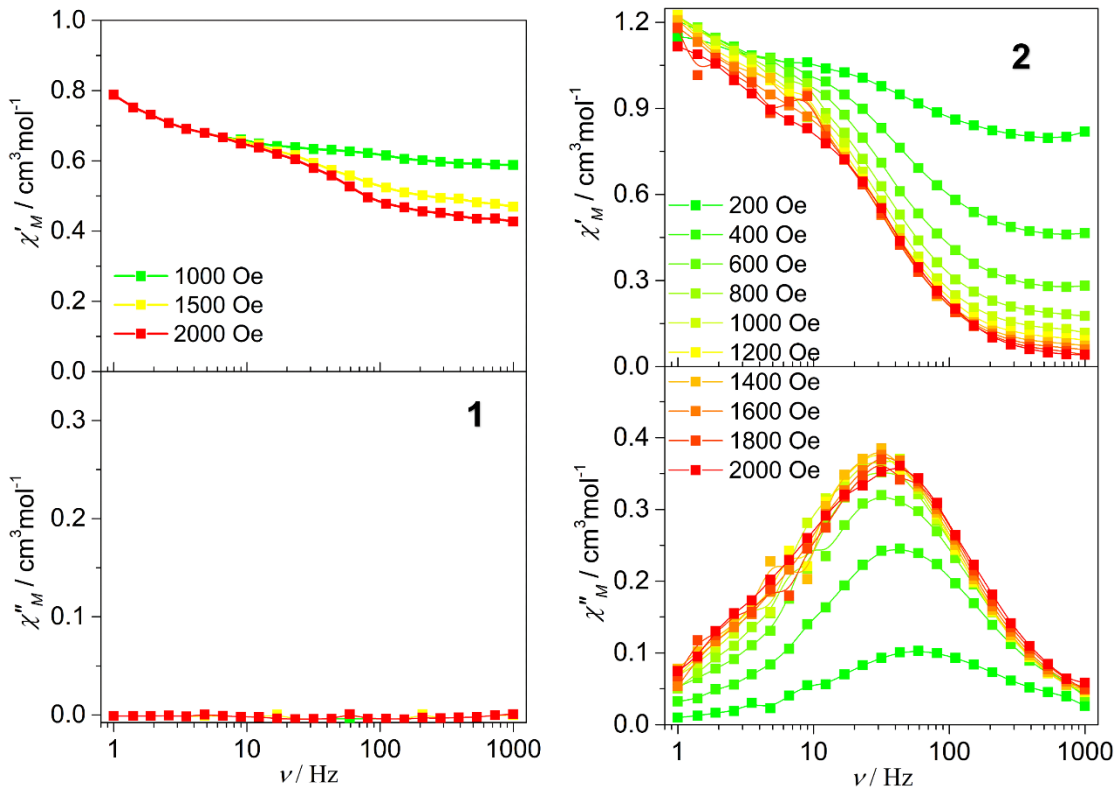


Figure S10. Frequency dependence of the in-phase (χ') and out-of-phase (χ'') part of the ac susceptibilities measured under various dc fields at 1.8 K for **1** and **2**.

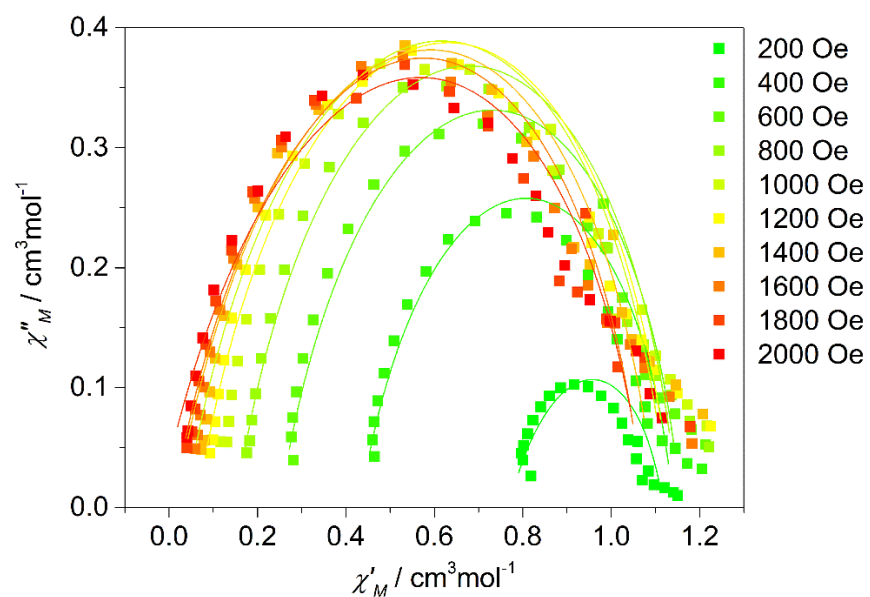


Figure S11. Cole-cole plot for **2** under various dc fields at 1.8 K.

Table S4. Relaxation fitting parameters at 1.8 K under different fields from the least-square fitting of the Cole-Cole plots of **2** according to the generalized Debye model.

H / Oe	$\chi_S / \text{cm}^3\text{mol}^{-1}\text{K}$	$\chi_T / \text{cm}^3\text{mol}^{-1}\text{K}$	τ / s	α
200	0.76868	1.1179	0.00408	0.18748
400	0.43224	1.13999	0.00445	0.19895
600	0.25001	1.15722	0.00534	0.20896
800	0.15061	1.1499	0.00586	0.2181
1000	0.0185	1.15744	0.00271	0.22298
1200	0.06303	1.13473	0.0064	0.22101
1400	0.0361	1.12751	0.00638	0.21248
1600	0.01367	1.09937	0.00598	0.20411
1800	0.00813	1.07237	0.0057	0.19149
2000	0.00232	1.07723	0.00572	0.18356

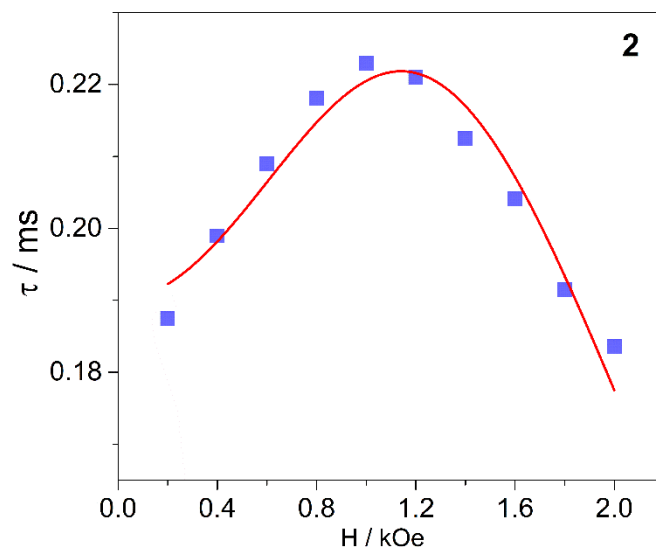


Figure S12. Field dependence of the magnetic relaxation time at 1.8 K for **2** and its approximation by $\tau^{-1} = AH^2T + B_1/(1 + B_2H^2)$. The best fit gives $A = 0.95$, $B_1 = 5.26$, and $B_2 = 0.47$.

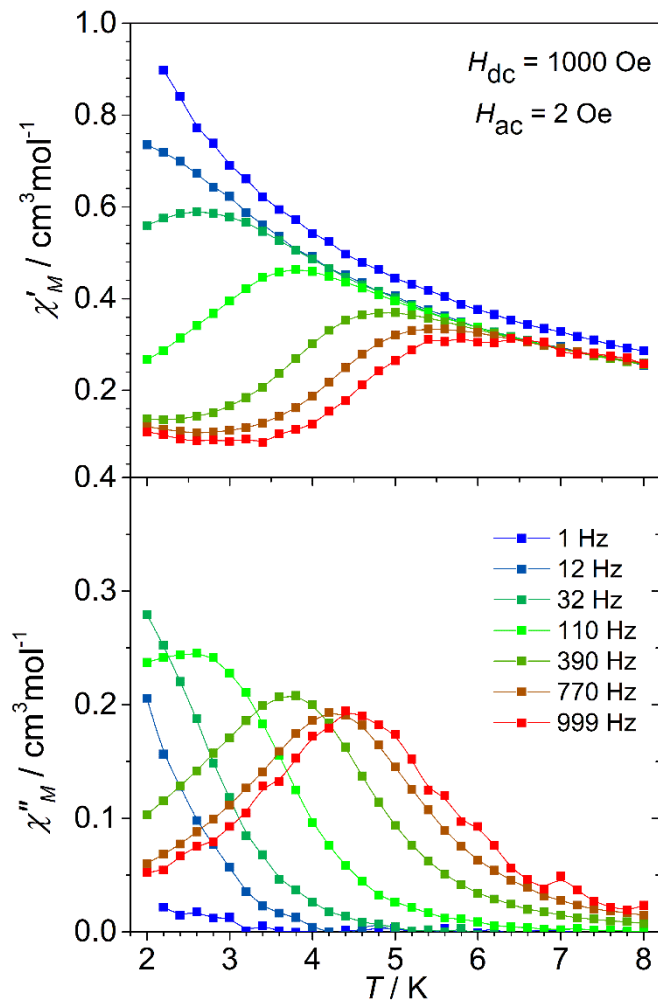


Figure S13. Temperature dependence of the in-phase (χ') and out-of-phase (χ'') part of the ac susceptibilities measured under 1 kOe dc field for **2**.

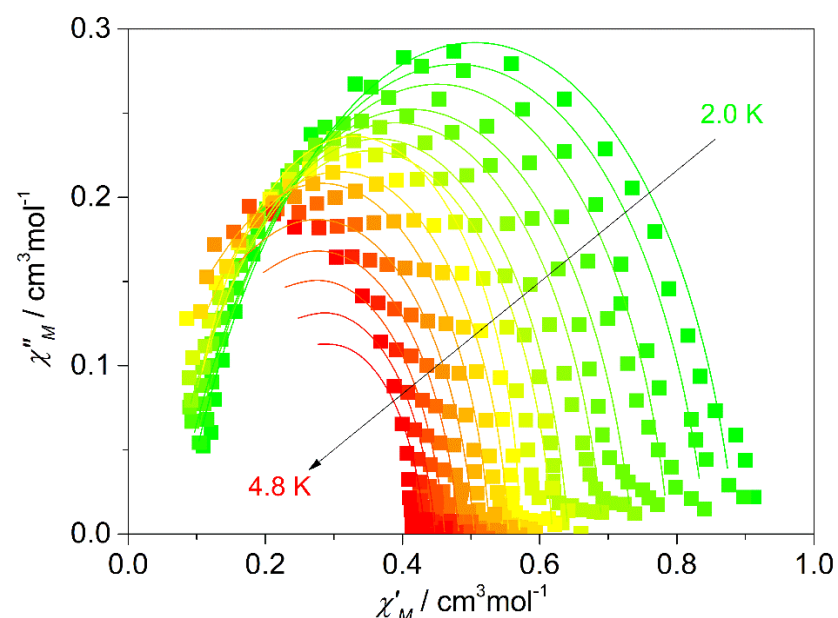


Figure S14. Cole-cole plot for **2** under various dc fields at 1.8 K.

Table S5. Relaxation fitting parameters from the least-square fitting of the Cole-Cole plots of **2** according to the generalized Debye model.

T / K	τ / s	χ_s / $\text{cm}^3\text{mol}^{-1}\text{K}$	χ_T / $\text{cm}^3\text{mol}^{-1}\text{K}$	α
2.0	0.07606	0.88559	0.00402	0.1996
2.2	0.06615	0.84228	0.00339	0.20167
2.4	0.07447	0.7883	0.00264	0.17648
2.6	0.0512	0.73492	0.00196	0.18538
2.8	0.05591	0.69178	0.00157	0.16017
3.0	0.06494	0.64145	0.00121	0.12316
3.2	0.06699	0.61862	1E-3	0.1147
3.4	0.08701	0.57057	7.6E-4	0.00478
3.6	0.04813	0.5546	5.6E-4	0.09579
3.8	0.01986	0.52724	4.3E-4	0.11782
4.0	0.02392	0.50464	3.4E-4	0.15295
4.2	0.05098	0.48205	2.8E-4	0.15058
4.4	0.07126	0.46142	2.3E-4	0.15673
4.6	0.11075	0.44732	2.2E-4	0.15016
4.8	0.1414	0.43242	1.9E-4	0.15564

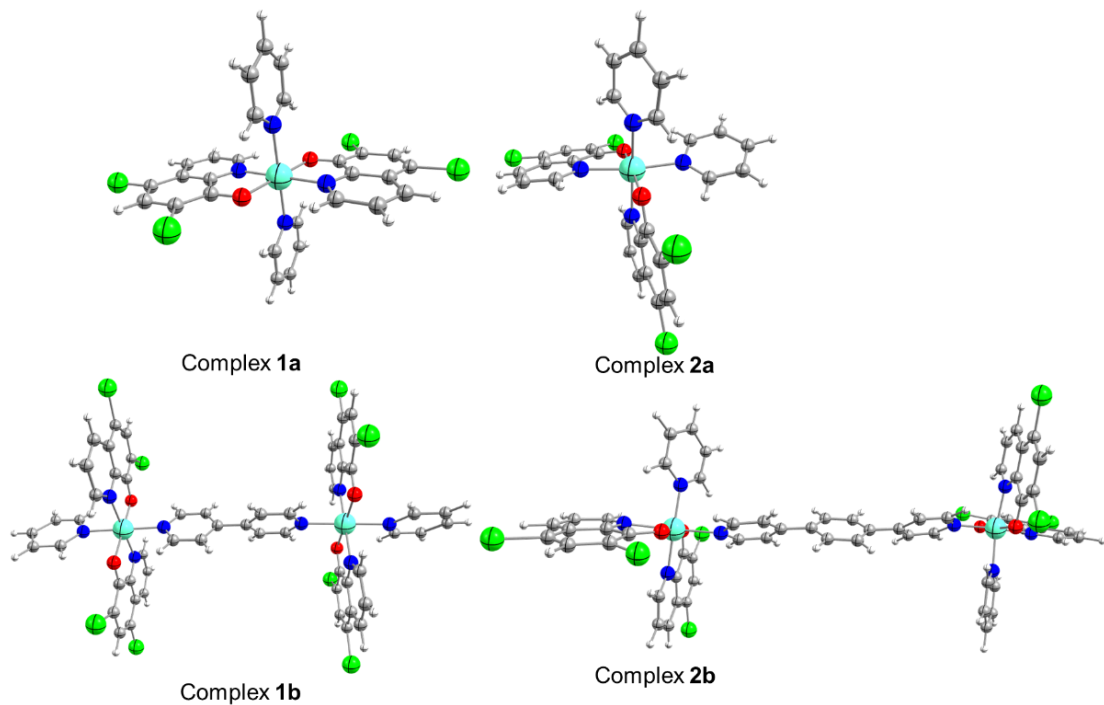
Computational Methods.

Figure S15. Monomeric (top) and Dimeric (bottom) models extracted from the crystal structure of complexes **1** and **2**. The position of hydrogens was optimized using DFT calculations. Colour code: light blue, Co; dark blue, N; red, O; green, Cl; grey, C; white, H)

Table S6. CASSCF/NEVPT2 computed 10 spin-free quartets (red) and 40 spin-free doublet (black) states along with the spin-orbit states for **1a**. All the values are reported here in cm⁻¹

Complex 1a							
SPIN-FREE STATES				SPIN-ORBIT		STATES	
CASSCF	NEVPT2	CASSCF	NEVPT2	CASSCF	NEVPT2	CASSCF	NEVPT2
0.0	38474.0	0.0	39272.2	0.0	31503.2	0.0	30854.5
653.0	38602.2	930.2	39976.3	171.0	31887.0	137.3	31621.6
996.0	47616.1	1427.7	41642.9	753.5	33306.3	991.2	32680.1
7845.5	47752.6	10357.2	41796.6	1059.0	33917.3	1235.4	33532.7
8522.7	48418.8	11088.1	42625.7	1354.8	36467.9	1690.0	35985.4
9016.9	49201.0	11829.4	45061.6	1459.3	36892.1	1792.1	36483.7
17546.6	49945.1	22457.4	45852.1	8108.5	37216.9	7988.2	36990.8
23969.7	50218.2	22317.6	46489.8	8163.2	37615.2	9226.4	37546.1
25742.3	50427.9	24545.0	45839.1	8783.6	38307.1	10542.6	38777.5
25905.1	72890.3	24721.0	64315.1	8839.4	38613.7	10603.6	39571.5
12962.9	73577.9	7722.4	65361.3	9285.9	38821.1	11271.4	40020.4
13976.4	73679.5	8971.9	65478.2	9372.2	39170.8	11334.8	40384.4
19670.1	75261.3	17306.5	67325.7	13253.2	47754.4	12011.8	41748.0
20154.6	75298.1	18072.1	67417.0	14264.2	48171.5	12100.3	42165.4
20269.1		18269.8		17856.6	48786.8	17488.7	42938.8
20407.4		18390.9		17860.7	49504.7	18176.2	45308.0
20708.8		18807.8		19868.2	50204.9	18557.8	46069.3
21239.8		19566.8		20274.5	50612.8	18724.5	46123.2
25747.2		21915.9		20658.4	50764.0	19133.9	46792.3
26266.8		26160.0		20802.2	73205.0	19894.1	64582.7
26342.4		23471.7		21105.6	73856.5	21701.0	65582.4
26481.8		22972.3		21659.0	74083.0	22380.2	65824.3
29577.3		28710.2		24057.2	75435.0	22642.3	67463.5
29836.0		28663.6		24175.6	75823.1	22701.0	67861.9
30538.3		30074.4		25501.0		22828.3	
30588.2		30035.8		25704.4		23022.9	
31181.4		30591.8		25860.8		23732.4	
31594.5		31394.9		26070.7		24611.7	
32966.7		32397.2		26374.4		24869.6	
33579.4		33259.8		26696.5		25122.6	
36256.0		35812.4		27073.3		25329.8	
36647.3		36240.6		27435.0		26501.7	
37061.0		36854.9		29895.4		28869.9	
37237.5		37135.3		30241.0		29113.7	
37698.2		38367.2		30823.4		30264.5	
38224.5		39764.7		30964.9		30377.1	

Table S7. CASSCF/NEVPT2 computed 10 spin-free quartets (red) and 40 spin-free doublet (black) states along with the spin-orbit states for **2a**. All the values are reported here in cm⁻¹

Complex 2a							
SPIN-FREE STATES				SPIN-ORBIT		STATES	
CASSCF	NEVPT2	CASSCF	NEVPT2	CASSCF	NEVPT2	CASSCF	NEVPT2
0.0	37734.1	0.0	38411.3	0.0	31106.0	0.0	30387.0
340.0	37823.6	414.6	38647.8	214.1	31202.2	198.5	30637.2
1200.7	47260.5	1637.8	41145.8	618.4	32753.4	673.0	31838.6
7755.2	47470.5	10131.5	41442.4	905.8	33555.0	918.2	32970.4
8021.9	48321.6	10474.8	42707.4	1580.6	35824.3	1955.9	35037.2
8284.0	48744.8	10647.4	44290.6	1646.3	36291.2	2019.2	35812.5
16765.7	49619.4	21434.9	45174.9	8074.8	36714.6	8102.3	36275.1
23091.4	49849.5	21052.3	45260.5	8128.8	37164.3	10259.0	36892.9
25436.5	50018.7	24051.0	45621.1	8343.5	37780.9	10400.7	38323.8
25906.8	72210.7	24578.3	63268.7	8394.4	37944.2	10487.7	38629.9
12965.2	73324.1	7755.5	65023.9	8629.6	38150.6	10733.1	38806.4
14711.4	73584.6	9961.9	65265.4	8740.9	38538.9	10782.8	39218.9
19627.4	74573.7	17359.3	66212.4	13319.3	47491.1	10942.8	41382.5
19808.8	74795.9	17558.4	66351.8	15058.8	47945.6	11068.8	41870.7
19954.6		17791.9		17148.5	48737.2	17569.9	43083.7
20727.1		18721.8		17150.2	49119.3	17855.5	44629.4
20881.7		19001.8		19847.7	49932.8	18188.6	45495.9
21114.2		19333.3		20107.3	50307.0	19056.7	45592.2
25710.5		22029.6		20413.2	50429.6	19411.7	46032.9
25844.2		22150.5		21094.8	72607.0	19741.4	63635.4
25959.0		23041.4		21360.3	73646.0	21045.4	65306.8
26425.2		26275.3		21589.5	74034.1	21243.6	65682.7
29450.5		28204.4		23293.0	74959.6	21764.6	66545.2
29843.7		28618.6		23383.1	75267.2	21777.9	66813.3
30009.5		28951.4		25371.6		22388.1	
30583.7		29946.8		25582.0		22575.0	
30732.3		30049.9		25707.0		23209.8	
30836.6		30314.6		26025.2		24317.2	
32343.0		31464.6		26232.8		24501.6	
33148.0		32605.0		26583.6		24984.5	
35534.8		34748.3		26794.7		25170.0	
36089.3		35642.4		27355.9		26662.6	
36292.2		35806.9		29834.0		28557.2	
36735.6		36460.4		30257.7		29013.9	
37229.9		37886.6		30486.3		29372.4	
37520.3		38318.6		30962.6		30279.7	

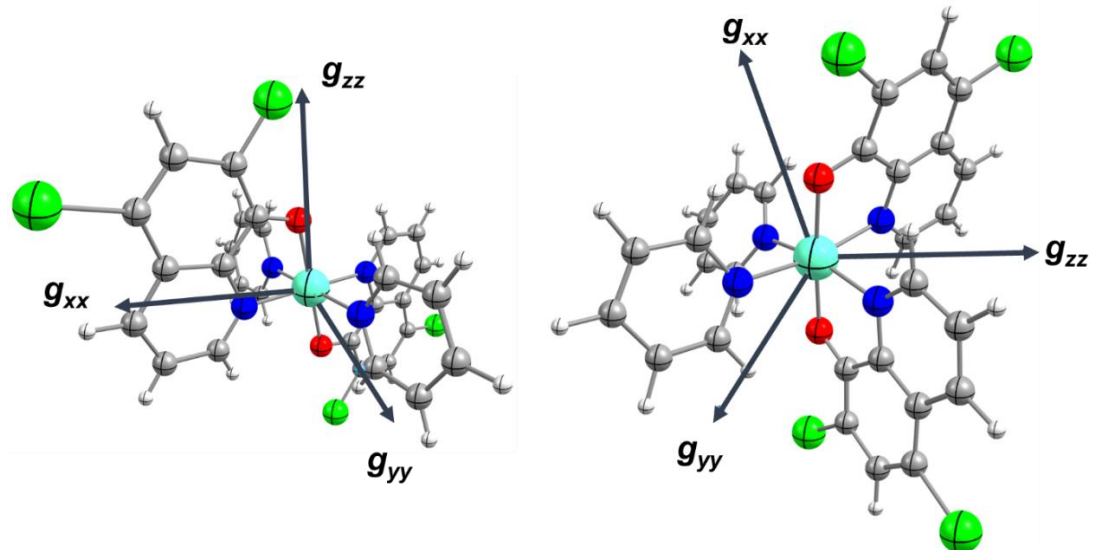


Figure S16. Orientation of computed effective g-tensor of complex **1a** and **2a**.

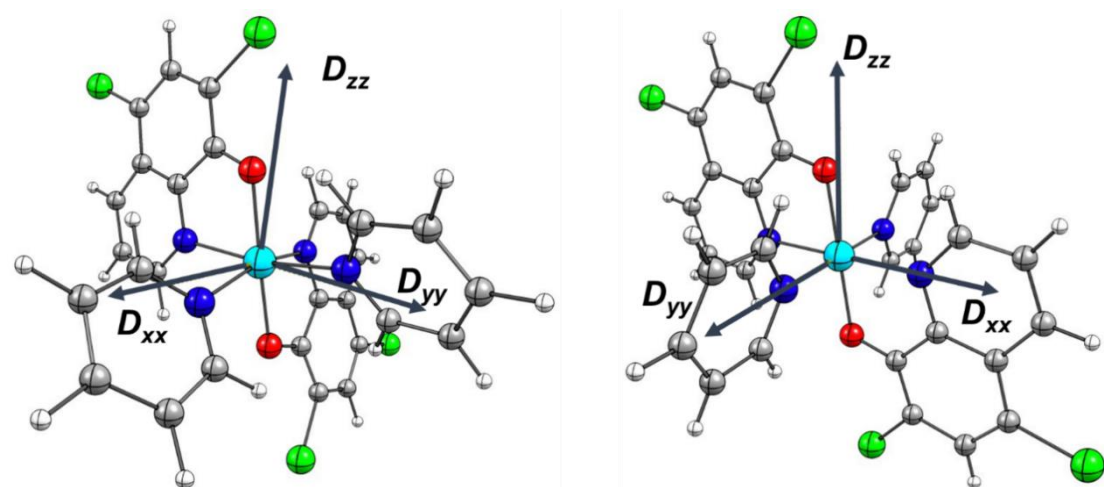


Figure S17. Orientation of computed D-tensor of complex **1a** and **2a**.

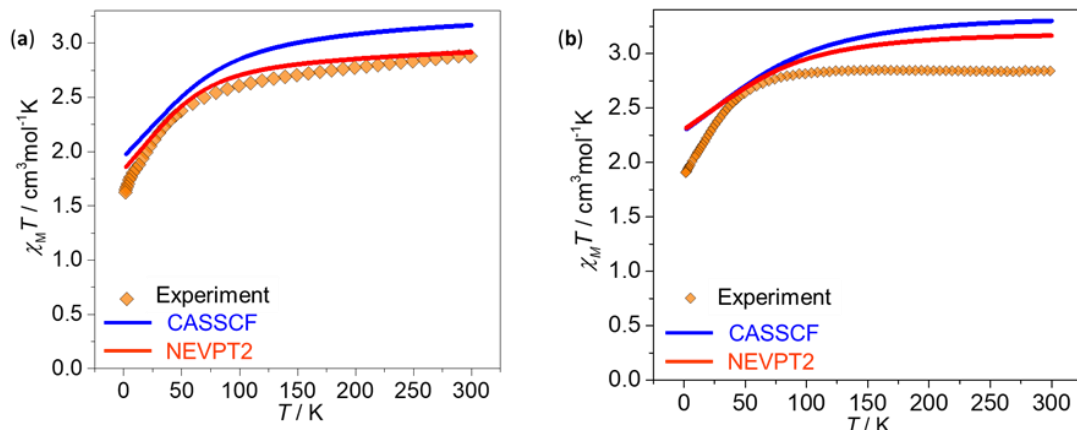


Figure S18. Experimental and *ab initio* computed magnetic susceptibility plots for complexes (a) **1** and (b) **2** where yellow diamonds correspond to the experimental values and the blue and red lines correspond to CASSCF and NEVPT2 computed values, respectively. All these computed values are obtained from the calculations on monomeric model complexes **1a** and **2a**.

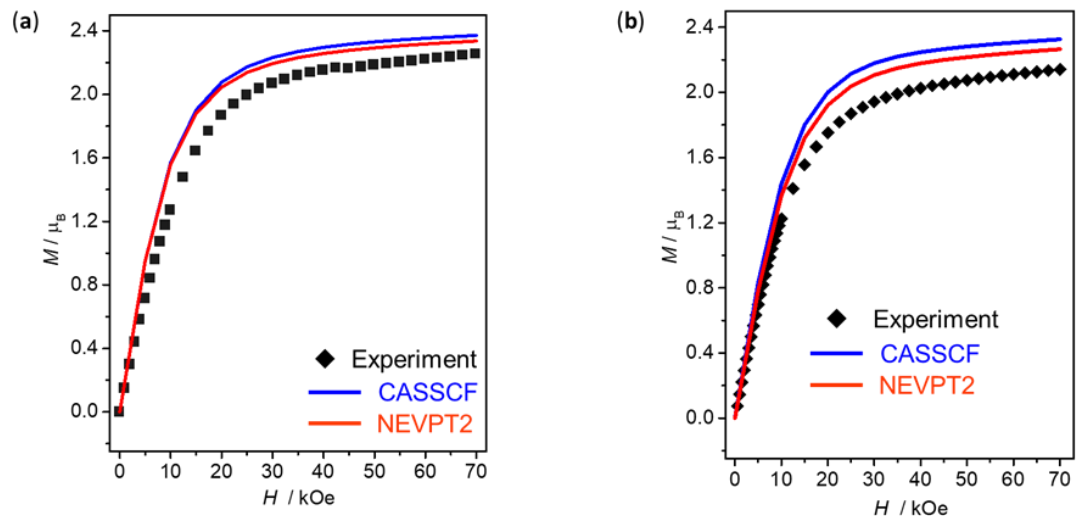


Figure S19. Experimental and *ab initio* computed magnetization curves at 2 K (a) **1** and (b) **2**. The black squares represent the experimental values, and the blue and red lines correspond to CASSCF and NEVPT2 computed values. All these computed values are obtained from the calculations on monomeric model complexes **1a** and **2a**.

Table S8. CASSCF (7,5)+NEVPT2 computed Spin–Hamiltonian parameter (g , D , $|E/D|$) parameters along with wavefunction decomposition analysis.

Parameters		1a		2a	
		CASSCF	NEVPT2	CASSCF	NEVPT2
D	EHA	81.56	65.35	-94.62	-91.19
	2PT	93.19	72.13	-193.15	-162.05
E/D	EHA	0.18	0.19	0.31	0.25
	2PT	0.25	0.22	0.12	0.12
g_{xx}		1.9238	1.9573	1.8657	1.8963
g_{yy}		2.4678	2.3998	2.2473	2.203
g_{zz}		2.8075	2.6923	3.0376	2.9994
		KD1: 52% 3/2; ±1/2⟩ + 33% 3/2; ±3/2⟩	KD1: 52% 3/2; ±1/2⟩ + 41% 3/2; ±3/2⟩	KD1: 61% 3/2; ±1/2⟩ + 32% 3/2; ±3/2⟩	KD1: 62% 3/2; ±3/2⟩ + 32% 3/2; ±1/2⟩
g_{xx}		2.0352	1.8815	1.6667	1.3672
g_{yy}		3.5285	3.4068	2.1386	1.7384
g_{zz}		6.7731	6.5936	8.117	8.2879
		KD1: 54% 3/2; ±1/2⟩ + 41% 3/2; ±3/2⟩	KD2: 55% 3/2; ±3/2⟩ + 40% 3/2; ±1/2⟩	KD1: 62% 3/2; ±1/2⟩ + 33% 3/2; ±3/2⟩	KD2: 62% 3/2; ±1/2⟩ + 32% 3/2; ±3/2⟩
g_{xx}		1.3723	1.3167	2.2177	2.584
g_{yy}		1.4653	1.4362	2.8429	2.9735
g_{zz}		5.451	5.6339	4.5777	4.6257

EHA : Effective Hamiltonian approach ;2PT : Second order perturbation Theory

Table S9. AILFT derived ligand field parameters computed at CASSCF (in parentheses) and NEVPT2 level of theory for model complexes **1a** and **2a**. The values of *B*, *C*, ξ and Δ_o parameters are provided in units of cm⁻¹.

Parameter	Free Co(II)	1a	2a	% reduction	
				1a	2a
ξ	527	515.5	515.6	2.1	2.1
<i>B</i>	1040.3	1013.9	1008.4	2.5	3.0
	(1251.9)	(1194.7)	(1195.4)	(4.5)	(4.5)
<i>C</i>	4157.7	3801.3	3819.1	8.5	8.1
	(4621.1)	(4427.9)	(4428.6)	(4.1)	(4.1)
C/B	3.997	3.749	3.787	6.2	5.2
	(3.691)	(3.706)	(3.705)	(-0.4)	(-0.3)
Δ_o		19206.6	17777.1		
		(17565.3)	(16308.9)		

$$\% \text{ reduction} = 1 - \left(\frac{\text{complex}}{\text{free Co(II)}} \right) \times 100$$

Table S10. BS-DFT computed energies of high-spin and broken-symmetry solution of complex **1b** using H=-JS₁S₂ formalism.

Solution	Energy (E _h)	ρ ^{Co1}	ρ ^{Co2}	<S**2>	J (cm ⁻¹)
HS	-9373.721866933156	2.6935	2.6936	12.0303	-0.16
BS1	-9373.721869165391	-2.6935	2.6935	3.0304	

J values are estimated using the following equation,

$$J = \frac{E_{BS} - E_{HS}}{s_1 s_2 + \frac{s_2}{2}}$$

Table S11. BS-DFT computed energies of high-spin and broken-symmetry solution of complex **2b** using H=-JS₁S₂ formalism.

Solution	Energy (E _h)	ρ ^{Co1}	ρ ^{Co2}	<S**2>	J (cm ⁻¹)
HS	-9604.822227118952	2.6901	2.6901	12.0260	-0.009
BS1	-9604.822227251665	-2.6901	2.6901	3.0260	

J values are estimated using the following equation,

$$J = \frac{E_{BS} - E_{HS}}{s_1 s_2 + \frac{s_2}{2}}$$

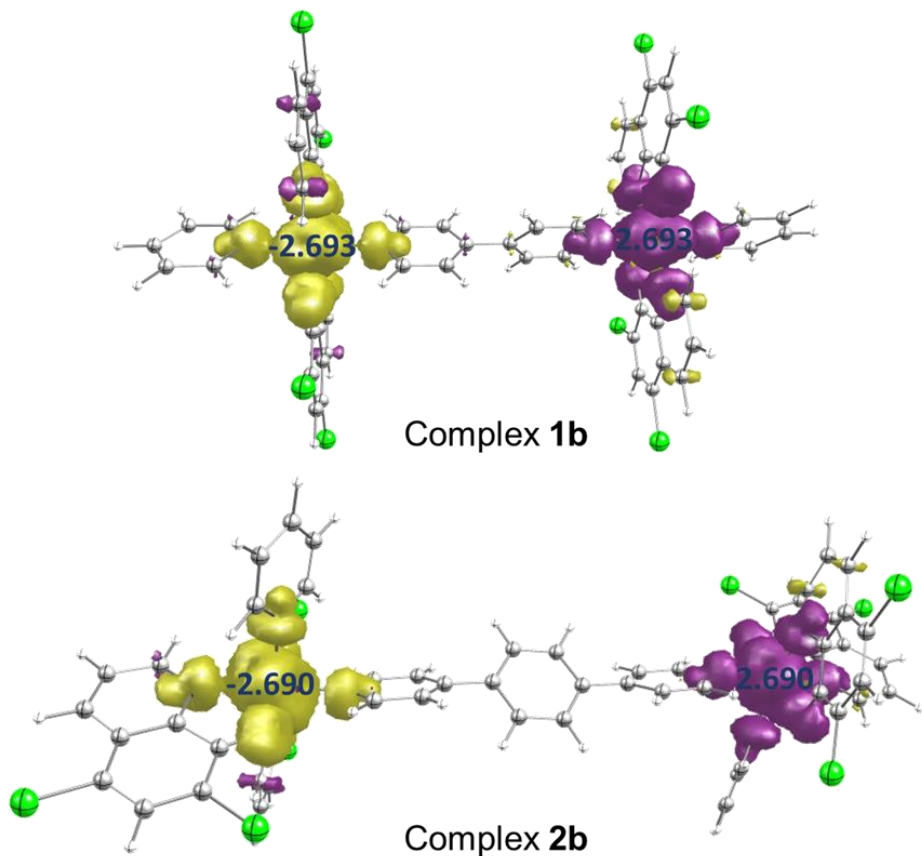


Figure S20. DFT calculated spin-density plot for the ground state ($S=0$) of complexes **1b** and **2b**; the positive and negative spin densities are represented by violet and yellow colour, respectively. The isodensity surface represented here corresponds to a value of $0.001 \text{ e}^-/\text{bohr}^3$.

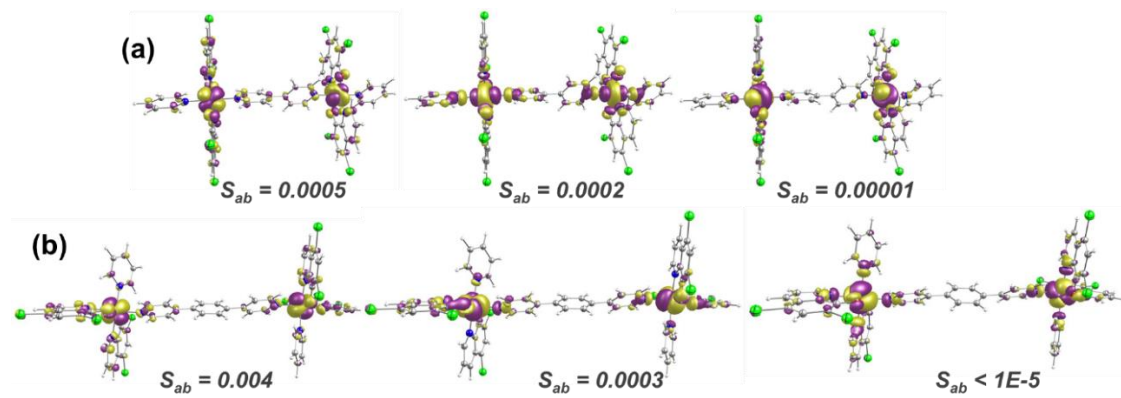


Figure S21. DFT calculated overlap integrals for complexes (a) **1b** and (b) **2b**. The isodensity surface represented here corresponds to a value of $0.01 \text{ e}^-/\text{bohr}^3$

Reference

- (1) SAINT Software Users Guide, version 7.0; Bruker Analytical Xray Systems: Madison, WI, **1999**.
- (2) Sheldrick, G. M. SADABS, version 2.03; Bruker Analytical X-ray Systems: Madison, WI, **2000**.
- (3) Sheldrick, G. M. SHELXTL, version 6.14; Bruker AXS, Inc.: Madison, WI, **2000–2003**.
- (4) Dolomanov, O. V.; Bourhis, L. J.; Gildea, R. J.; Howard, J. A. K.; Puschmann, H. OLEX2: A Complete Structure Solution, Refinement and Analysis Program. *J. Appl. Crystallogr.* **2009**, *42* (2), 339–341.
- (5) Neese, F. Software Update: The ORCA Program System, Version 4.0. *Wiley Interdiscip. Rev. Comput. Mol. Sci.* **2018**, *8*, 1–6.
- (6) Neese, F.; Wennmohs, F.; Becker, U.; Ripplinger, C. The ORCA Quantum Chemistry Program Package. *J. Chem. Phys.* **2020**, *152*.
- (7) Becke, A. D. Density-Functional Exchange-Energy Approximation with Correct Asymptotic Behaviour. *Phys. Rev. A* **1988**, *38*, 3098–3100.
- (8) Perdew, J. P. Density-Functional Approximation for the Correlation Energy of the Inhomogeneous Electron Gas. *Phys. Rev. B* **1986**, *33*, 8822–8824.
- (9) Weigend, F.; Ahlrichs, R. Balanced Basis Sets of Split Valence, Triple Zeta Valence and Quadruple Zeta Valence Quality for H to Rn: Design and Assessment of Accuracy. *Phys. Chem. Chem. Phys.* **2005**, *7*, 3297–3305.
- (10) Becke, A. D. A New Mixing of Hartree-Fock and Local Density-Functional Theories. *J. Chem. Phys.* **1993**, *98*, 1372–1377.
- (11) Grimme, S.; Antony, J.; Ehrlich, S.; Krieg, H. A Consistent and Accurate Ab Initio Parametrization of Density Functional Dispersion Correction (DFT-D) for the 94 Elements H-Pu. *J. Chem. Phys.* **2010**, *132*.
- (12) Grimme, S.; Ehrlich, S.; Lars, G. Effect of the Damping Function in Dispersion Corrected Density Functional Theory. *J. Comput. Chem.* **2011**, *32*, 1456–1465.
- (13) Noddeman, L. Valence Bond Description of Antiferromagnetic Coupling in Transition Metal Dimers. *J. Chem. Phys.* **1981**, *74*, 5737–5743.
- (14) Izsák, R.; Neese, F. Speeding up Spin-Component-Scaled Third-Order Perturbation Theory with the Chain of Spheres Approximation : The COSX-SCS-MP3 Method. *Mol. Phys.*, **2013**, *111*, 1190–1195.
- (15) Ruiz, E.; Cano, J.; Alvarez, S.; Alemany, P. Broken Symmetry Approach to Calculation of Exchange Coupling Constants for Homobinuclear and Heterobinuclear Transition Metal Complexes. *J. Comput. Chem.* **1999**, *20*, 1391–1400.
- (16) Singh, S. K.; Tibrewal, N. K.; Rajaraman, G. Density Functional Studies on Dinuclear {NiIIGdIII} and Trinuclear {NiIIGdIIINiII} Complexes: Magnetic Exchange and Magneto-Structural Maps. *Dalt. Trans.* **2011**, *40*, 10897–10906.
- (17) Piligkos, S.; Rajaraman, G.; Soler, M.; Kirchner, N.; Van Slageren, J.; Bircher, R.; Parsons, S.; Güdel, H. U.; Kortus, J.; Wernsdorfer, W.; Christou, G.; Brechin, E. K. Studies of an Enneanuclear Manganese Single-Molecule Magnet. *J. Am. Chem. Soc.* **2005**, *127*, 5572–5580.

- (18) Ruiz, E.; Cano, J.; Alvarez, S.; Caneschi, A.; Gatteschi, D. Theoretical Study of the Magnetic Behavior of Hexanuclear Cu(II) and Ni(II) Polysiloxanolato Complexes. *J. Am. Chem. Soc.* **2003**, *125*, 6791–6794.
- (19) Singh, S. K.; Vignesh, K. R.; Archana, V.; Rajaraman, G. Theoretical Insights into the Origin of Magnetic Exchange and Magnetic Anisotropy in {Re^{IV}-M^{II}} (M = Mn, Fe, Co, Ni and Cu) Single Chain Magnets. *Dalt. Trans.* **2016**, *45*, 8201–8214.
- (20) Christian, P.; Rajaraman, G.; Harrison, A.; Helliwell, M.; McDouall, J. J. W.; Raftery, J.; Winpenny, R. E. P. Synthesis and Studies of a Trinuclear Mn(II) Carboxylate Complex. *Dalt. Trans.* **2004**, *16*, 2550–2555.
- (21) Caballero-Jiménez, J.; Habib, F.; Ramírez-Rosales, D.; Grande-Aztatzi; Rafael; Merino, G.; Korobkov, I.; Singh, M. K.; Rajaraman, G.; Reyes-Ortegaa, Y.; Murugesu, M. Inducing Magnetic Communication in Caged Dinuclear Co(II) Systems. *Dalt. Trans.* **2015**, *44*, 8649–8659.
- (22) M. Llunell, D. Casanova, J. Cirera, P. Alemany, S. Alvarez, SHAPE, Version 2.1. Universitat de Barcelona, **2013**.